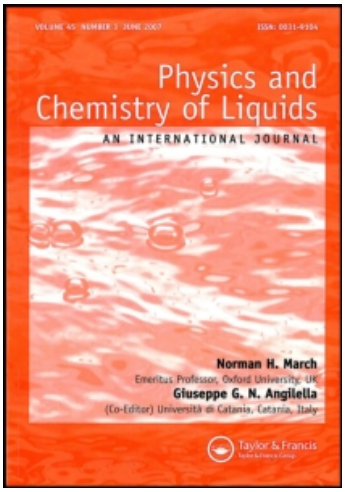

Physics and Chemistry of Liquids
Publication details, including instructions for authors and subscription information:
http://www.informaworld.com/smpp/title~content=t713646857

Chemical Order of Manganese-Antimony Liquid Alloys Obtained Experimentally by the Neutron "Null Matrix" Method

B. Grosdidier[a]; J. L. Bos[a]; J. G. Gasser[a]; R. Bellissent[b]
[a] Laboratoire de Physique des Liquides et des Interfaces, Institut de Physique-électronique et de Chimie, Université de Metz, Metz Cedex 3, France [b] Laboratoire Léon Brillouin CEA-CNRS, Gif-suf-Yvette Cedex, France

Online publication date: 27 October 2010

To cite this Article Grosdidier, B. , Bos, J. L. , Gasser, J. G. and Bellissent, R.(2002) 'Chemical Order of Manganese-Antimony Liquid Alloys Obtained Experimentally by the Neutron "Null Matrix" Method', Physics and Chemistry of Liquids, 40: 5, 553 — 580
To link to this Article: DOI: 10.1080/0031910029001/0491
URL: http://dx.doi.org/10.1080/0031910029001/0491

Phys. Chem. Liq., 2002, Vol. 40(5), pp. 553–580

Taylor & Francis
Taylor & Francis Group

CHEMICAL ORDER OF MANGANESE–ANTIMONY LIQUID ALLOYS OBTAINED EXPERIMENTALLY BY THE NEUTRON "NULL MATRIX" METHOD

B. GROSDIDIER[a,*], J.L. BOS[a], J.G. GASSER[a] and R. BELLISSENT[b]

[a]*Laboratoire de Physique des Liquides et des Interfaces, Institut de Physique-électronique et de Chimie, Université de Metz. CP87811, 1 Boulevard D.F. Arago, 57078 Metz Cedex 3, France;* [b]*Laboratoire Léon Brillouin CEA-CNRS C.E. Saclay-91191 Gif-suf-Yvette, Cedex, France*

(Received 31 December 2001)

The Bhatia–Thornton concentration–concentration partial structure factor $S_{CC}(q)$ is a strong indicator of the order in liquid alloys. Manganese is one of the four metals, which has a negative neutronic scattering length, while the antimony one is positive. Thus for a defined composition ($Mn_{60}Sb_{40}$) the linear combination of the two neutronic scattering lengths weighted by the atomic compositions is zero (zero alloy). We present here the results of neutron diffraction on the $Mn_{60}Sb_{40}$ "null matrix" alloy at 950°C, which is proportional to the Bhatia–Thornton $S_{CC}(q)$ ("null matrix" method). The total structure factor of $Mn_{40}Sb_{60}$ at 800°C has also been measured. The main peak of the experimental $S_{CC}(q)$ is a proof of a strong chemical order in this alloy. This order is confirmed in the real space by the Fourier transform of the structure factor. To interpret our experimental results, one generally uses effective potentials determined with the pseudopotential formalism. But transition metal pseudopotentials are not easy to handle especially in alloys. We used different simple effective potential models: hard spheres with constant diameters, hard spheres with composition dependent diameters, shouldered hard spheres models. We first show that the hard sphere model cannot reproduce the experimental results if we postulate that the hard sphere diameters do not change on alloying. Then we fit the hard sphere diameters on the experimental structure factor of the alloy. This schema can correspond physically to a charge transfer between the two components. We show that it can no more explain the experiment. The addition of attractive and (or) repulsive contributions to the different interatomic potentials give

*Corresponding author. Tel.: +33 3 87 31 58 80. Fax: +33 3 87 31 58 84.
E-mail: benoitg@lpli.sciences.univ-metz.fr

ISSN 0031-9104. Online ISSN: 1029-0451
DOI: 10.1080/0031910029001/0491

satisfactory results. The best results are obtained with attractive contributions between unlike atoms and repulsive ones between identical atoms. We have also shown that the parameters obtained for $Mn_{60}Sb_{40}$ give also good results for the structure factor at a second composition: $Mn_{40}Sb_{60}$.

Keywords: "Null-matrix" method; Heterocoordination; Interatomic potential; liquid alloy; atomic structure; Mn–Sb

1 INTRODUCTION

The electrical resistivity of liquid Mn–Sb alloys was measured by Gasser and Kleim [1] and more recently the thermopower by Benazzi [2]. The resistivity presents a maximum (250 μΩ cm) and a negative temperature coefficient for a 40 at.% antimony composition. In the frame of the extended Faber–Ziman theory of Dreirach *et al.* [3], the resistivity is expressed as an integral of the product of two factors more or less independent: the form factor and the structure factor (weighted by a q^3 term) which may explain this maximum. The first effect comes from the metals form factors and their behaviour *versus* concentration. The second arises from the structure factor with a short-range order, which can be characterised by the Bhatia–Thornton concentration–concentration partial structure factor $S_{CC}(q)$. With the neutronic scattering length of manganese and antimony, the experimental total structure factor $S(q)$ is directly proportional to the Bhatia–Thornton partial structure factor $S_{CC}(q)$ at 40 at.% concentration of antimony [4], where the maximum of the resistivity is also found. The relation is $S(q) = S_{CC}(q)/((1 - c_2)\, c_2)$ ($c_2 = 0.4$ is the antimony concentration). This is the so-called "NULL MATRIX" METHOD which has been used by Ruppersberg and Reiter for the lithium lead alloy [5]. Measurements have been done on the two axis spectrometer 7C2 built on the hot source of the reactor Orphée of the LLB at Saclay. We measured the structure factors of $Mn_{60}Sb_{40}$ at 950°C and of $Mn_{40}Sb_{60}$ at 800°C. In Section 2, we present the relations between the alloy total structure factor and the partial structure factors and the relations between partial structure factors $a_{ij}(q)$ and partial pair correlation functions $g_{ij}(r)$. We recall also the relationship between the effective ion–ion potentials and the structure of liquid alloys. The experimental setup, standard corrections and manganese magnetic scattering cor-

rection method are briefly described in Section 3. In Section 4, the experimental results are presented, discussed and compared to those obtained from the hard spheres and from the shouldered ion–ion potentials.

2 THEORY

2.1 Structure Factors and Pair Correlation Functions

We measure a total alloy structure factor $S_{\text{tot}}(q)$ that is bound to three sets of partial structure factors:

$$S_{\text{tot}}(q) = \frac{c_1 b_1^2 S_{11}(q) + 2\sqrt{c_1 c_2} b_1 b_2 S_{12}(q) + c_2 b_2^2 S_{22}(q)}{c_1 b_1^2 + c_2 b_2^2}, \tag{1}$$

where c_1, c_2, b_1, b_2 are respectively the concentrations and the neutron scattering lengths of each metal. $S_{ij}(q)$ are the Ashcroft–Langreth partial structure factors [6]. We have also:

$$S_{\text{tot}}(q) - 1 = \frac{c_1^2 b_1^2 (a_{11}(q) - 1) + 2c_1 c_2 b_1 b_2 (a_{12}(q) - 1) + c_2^2 b_2^2 (a_{22}(q) - 1)}{c_1 b_1^2 + c_2 b_2^2}. \tag{2}$$

The $a_{ij}(q)$ are the Faber–Ziman partial structure factors [7] and are connected to the partial pair correlation functions $g_{ij}(r)$ by:

$$g_{ij}(r) - 1 = h_{ij}(r) = \frac{1}{2\pi^2 \rho_0 r} \int_0^\infty q(a_{ij}(q) - 1) \sin(qr)\, dr, \tag{3}$$

where ρ_0 is the average number density.

The Eqs. (2) and (3) permit us to introduce the total pair correlation function $g_{\text{tot}}(r)$ whose expression is:

$$g_{\text{tot}}(r) - 1 = \frac{c_1^2 b_1^2 (g_{11}(r) - 1) + 2c_1 c_2 b_1 b_2 (g_{12}(r) - 1) + c_2^2 b_2^2 (g_{22}(r) - 1)}{c_1 b_1^2 + c_2 b_2^2}. \tag{4}$$

The total structure factor $S_{\text{tot}}(q)$ can also be written:

$$S_{\text{tot}}(q) = \frac{(c_1b_1 + c_2b_2)^2 S_{NN}(q) + 2(c_1b_1 + c_2b_2)(b_1 - b_2)S_{NC}(q) + (b_1 - b_2)^2 S_{CC}(q)}{c_1b_1^2 + c_2b_2^2}. \tag{5}$$

$S_{NN}(q)$, $S_{NC}(q)$ and $S_{CC}(q)$ are the Bhatia–Thornton partial structure factors [4]. When the quantity $c_1b_1 + c_2b_2$ is equal to 0, it can be shown that $S_{\text{tot}}(q) = S_{CC}(q)/(c_1c_2)$. The structure factor $S_{CC}(q)$ represents the fluctuations around the mean value c_1c_2 and can be written in function of the Faber–Ziman partial structure factors:

$$S_{CC}(q) = c_1c_2(1 + c_1c_2(a_{11}(q) + a_{22}(q) - 2a_{12}(q))). \tag{6}$$

The Fourier transform of $S_{\text{tot}}(q)$ is given by:

$$\frac{1}{2\pi^2\rho_0 r c_1 c_2}\int_0^\infty q\left(\frac{S_{CC}(q)}{c_1c_2} - 1\right)\sin(qr)\,dr = g_{11}(r) + g_{22}(r) - 2g_{12}(r) = \frac{g_{CC}(r)}{(c_1c_2)^2}. \tag{7}$$

The quantity $g_{11}(r) + g_{22}(r) - 2g_{12}(r)$ represents the difference between the homocoordination and the heterocoordination and indicates the nature of the chemical order in the alloy. In our case, the neutron scattering lengths of manganese and antimony are respectively equal to -3.730 and 5.641 fm, $c_1b_1 + c_2b_2 = 0$ for exactly $c_2 = 0.3981$ which is the "zero alloy". Only four 'natural' metals have a negative scattering length: lithium, titanium, vanadium and manganese. Thus, the study of alloys containing such a metal presents a strong interest but has not often been used [5].

2.2 Relations between the Structure and the Potential

In the alloys, the correlation functions are related by $g_{ij}(r) = h_{ij}(r) + 1$ and are given by the Ornstein–Zernike [8] equation:

$$h_{ij}(r) = c_{ij}(r) + \sum_{k=1}^{2}\rho_k\int_0^\infty c_{ik}\left(\left|\vec{r} - \vec{r}'\right|\right)h_{kj}(r)\,d^3\vec{r}' \qquad i,j = 2, \tag{8}$$

where ρ_k is the average number density of k-type atoms. The $c_{ij}(r)$ are the direct correlation functions between i and j particles, the second term of formula (8) describes the correlation between i and j through all atoms in the alloy. This equation can be written in the q momentum space:

$$h_{ij}(q) = c_{ij}(q) + \sum_{k=1}^{2} \rho_k c_{ik}(q) h_{kj}(q) \qquad i,j = 2, \tag{9}$$

Many equations can be used to link approximately the correlation functions to the ion–ion potentials $v_{ij}(r)$. For simple ion–ion effective potentials, it is convenient to use the Percus–Yevick equation [9]:

$$g_{ij}(r)\left(1 - \exp\frac{v_{ij}(r)}{k_B T}\right) = c_{ij}(r). \tag{10}$$

The structure of liquid metals has been calculated numerically by using the pseudopotential method. However, this method is not suitable to describe transition metals like manganese. To our knowledge, the direct correlation functions have been calculated with an analytical method for alloys only for few simple potentials: hard sphere potentials [6], Silbert–Young [10] potentials by Gopala Rao [11] and Yukawa potentials by Hafner *et al.* [12] (but only with equal hard sphere diameters). The Silbert–Young potential [10] permits to correct the hard sphere potential (which is the main effect) either by an attraction or by a repulsion between i and j particles. For a hard sphere pair potential, the function $c_{ij}(r)$ was determined for alloys by Lebowitz [13] and used by Ashcroft and Langreth [6]

$$v_{ij}(r) = \begin{cases} \infty & r < \sigma_{ij} \\ 0 & r > \sigma_{ij} \end{cases}, \tag{11}$$

$$-c_{ij}^{HS}(r) = \begin{cases} a_i & \lambda_{ij} > r > 0 \\ a_{ij} + b_{ij} r + d r^3 + \dfrac{f_{ij}}{r} & \lambda_{ij} < r < \sigma_{ij} \\ 0 & \sigma_{ij} < r \end{cases}, \tag{12}$$

σ_{ii} are the hard sphere diameters of the ith type metallic ion in the alloy, σ_i are the hard sphere diameters of the pure metal. We have also:

$$\sigma_{ij} = (\sigma_{ii} + \sigma_{jj})/2, \qquad \lambda_{ij} = (\sigma_{jj} - \sigma_{ii})/2, \qquad a_{ij} = (a_i + a_j)/2, \quad \text{and} \quad b_{ij} = (b_i + b_i)/2. \tag{13}$$

For a Silbert–Young pair potential, $c_{ij}(r)$ was given for alloys by Gopala Rao and Satpathy [11]. This model has been used by some of us [14] to explain the prepeak of the ternary Al–Ni–Si alloys.

$$v_{ij}(r) = \begin{cases} \infty \\ \varepsilon_{ij} \\ 0 \end{cases} \qquad c_{ij}^{HS}(r) = \begin{cases} c_{ij}^{HS}(r) & \sigma_{ij} > r \\ -v_{ij}(r)/k_B T = -\varepsilon_{ij}/k_B T & \sigma_{ij} < r < A_{ij}\sigma_{ij} \\ 0 & A_{ij}\sigma_{ij} < r \end{cases}. \tag{14}$$

It is well known that the interatomic potentials of metals have an oscillatory behaviour. In this work, we find necessary to add a second contribution identical to the first one, which is of the opposite sign. We called this potential "Double Step" potential. We obtain:

$$v_{ij}(r) = \begin{cases} \infty \\ \varepsilon_{ij} \\ \varepsilon'_{ij} \\ 0 \end{cases} \quad c_{ij}^{HS}(r) = \begin{cases} c_{ij}^{HS}(r) & \sigma_{ij} > r \\ -v_{ij}(r)/k_B T = -\varepsilon_{ij}/k_B T & \sigma_{ij} < r < A_{ij}\sigma_{ij} \\ -v'_{ij}(r)/k_B T = -\varepsilon'_{ij}/k_B T & A_{ij}\sigma_{ij} < r < A'_{ij}\sigma_{ij} \\ 0 & A'_{ij}\sigma_{ij} < r \end{cases}. \tag{15}$$

The possible shapes for this potential are represented on Figs. 1 and 2 where we compare our model to the effective potential that Koubaa and Gasser [15] obtained from the ab initio model potential of Bachelet, Hamann and Schlüter (B.H.S.) [16].

For the potential, the σ_{ij} and A_{ij} parameters have in general been determined by using the Lorenz-Berthelot interpolation rule:

$$\sigma_{ij} = \frac{\sigma_{ii} + \sigma_{jj}}{2} \qquad A_{ij}\sigma_{ij} = \frac{A_{ii}\sigma_{ii} + A_{jj}\sigma_{jj}}{2} \qquad \varepsilon_{ij} = \sqrt{\varepsilon_{ii}\varepsilon_{jj}}. \tag{16}$$

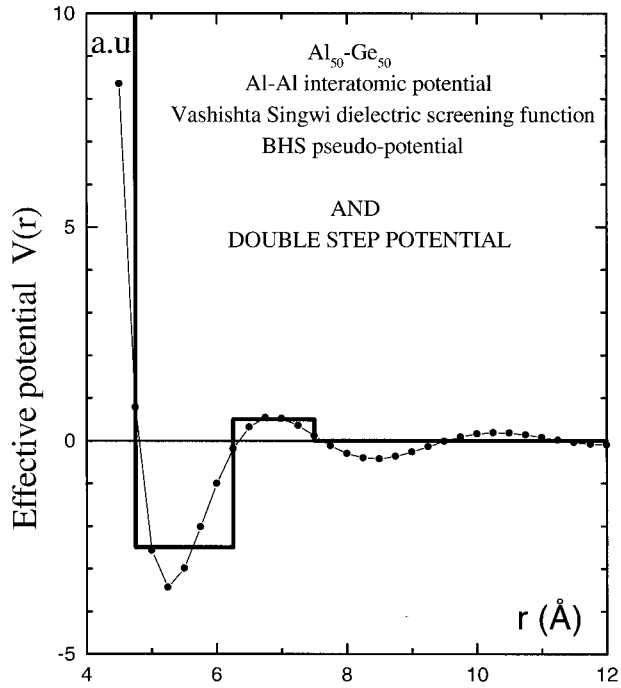

FIGURE 1 Characteristic attractive effective potential determined from Bachelet–Hamann–Schlüter (B.H.S.) pseudopotential calculations [15,16] (V_{Al-Al} in $Al_{50}Ge_{50}$ liquid alloy) and double step model for modelling this potential.

A strong chemical order necessarily transgresses the Lorentz–Berthelot rule. It is clear that our double step model potential, if the parameters are correctly adjusted on the true potential, includes most of the chemical interaction. The correct choice of the parameters will be discussed later.

3 EXPERIMENTAL SETUP

A complete description of the 7C2 spectrometer is given in [17]. We recall the main characteristics. The neutron beam section is equal to $5 \times 2\,cm^2$. The scattering wavevector is in the range from 0.3 to 16 $Å^{-1}$; our experimental wavelength is $\lambda \cong 0.707$ Å. The angular resolution and the number of cells are respectively equal to 0.2° and

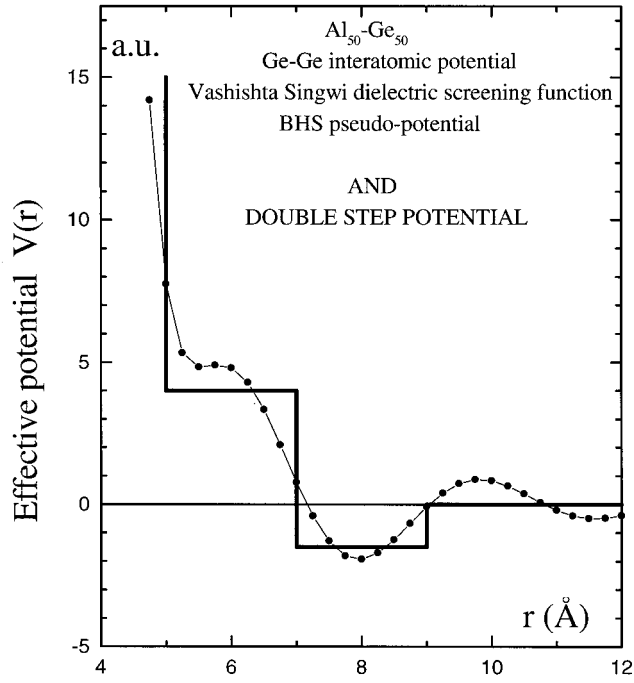

FIGURE 2 Characteristic repulsive effective potential determined from Bachelet–Hamann–Schlüter (B.H.S.) pseudopotential calculations [15,16] ($V_{Ge\text{–}Ge}$ in $Al_{50}Ge_{50}$ liquid alloy) and double step model for modelling this potential.

640. The highest neutron flux value is 2×10^7 neutrons $cm^{-2}\,s^{-1}$ at $\lambda \cong 0.707$ Å. The different alloys have been elaborated with metals of purity close to 99.999%.

We observed that manganese alloys sometimes react with silica cells at high temperatures. We think that this is mainly due to the presence of manganese oxide on the manganese flakes. In general, the presence of oxide does not influence the experiment, a small skin of oxide floats at the surface of the alloy but does not perturb the experiment. In our case, we took a special care to select manganese flakes without oxide and cleaned the flakes mechanically before preparing the alloy. An ingot was prepared before, by melting manganese and antimony. The alloy is cooled rapidly. The alloy is not homogenous. But we obtain an ingot of the desired shape which can be sealed in the silica cell.

When the experiment begins, we first heat the cell with the metal at the highest temperature possible. We take short spectra and follow the vanishing of the Bragg peaks which is an indicator of the melting of the alloy. We continue to measure short spectra (about 5–10 min). The 7C2 channel was monitored by a computer and a program written by the local contacts allows making ratio of the successive spectra. If the ratio is flat, it indicates that the liquid alloy is homogenous. At high temperature (up to 1000°C) we observed sometimes the appearance of a small peak in the ratio of spectra. This indicates that there is a drift, probably due to a chemical reaction with the silica cell. At smaller temperature this phenomenon does not occur but the alloy takes more time to melt and to be homogenous. The measurements with samples presenting this drift were rejected, or when the drift is very small we continue the experiment at a lower temperature. The experiment consists of several spectra at each temperature in order to have the desired statistical error. The ratio of spectra was systematically done in order to control the presence of an eventual drift. If no drift is observed the different spectra are added.

We used amorphous silica cells to contain the liquid alloys. They were placed in a vacuum furnace up to a temperature of 950°C. The absolute normalisation was made by using a vanadium rod, which presents the same geometric characteristics than the sample (cylinder with height and diameter respectively equal to 50 and 8 mm). Bellissent [18] has described the correction method for background, furnace, empty container effects, self-absorption and multiple scattering contributions. The neutron presents a magnetic interaction with manganese atoms due to the spin. A magnetic correction must be made. So we used the method of Ji-Chen Li *et al.* [19]. It consists in a subtraction of the paramagnetic cross section given by the usual formula (Bacon [20]):

$$\sigma_{p\mathrm{Mn}}(q) = \frac{8\pi}{3} S(S+1)\left(\frac{e^2\gamma}{mc^2}\right)^2 f_M^2(q), \tag{17}$$

where $f_M(q)$ is the magnetic form factor for the unpaired electrons and may be written:

$$f_M(q) = A\exp(-aq^2) + B\exp(-bq^2) + C. \tag{18}$$

The parameters of the previous formula are given in Ji-Chen Li's [19] Table I. A good magnetic correction involves an experimental $g(r) = 0$ at $r = 0$. After the magnetic correction, the total error on $S(q)$ is estimated $\cong 5\%$ at $q < 3\,\text{Å}^{-1}$ and $\cong 2\%$ for $q > 3\,\text{Å}^{-1}$. This leads to a total error equal to 10% on the total pair correlation function $g(r)$.

4 RESULTS AND DISCUSSION

4.1 Structure of the $Mn_{60}Sb_{40}$ Zero alloy

4.1.1 Experiment and the Hard Sphere Model

4.1.1.1 The Hard Sphere Diameters are Held Constant in the Alloy In Fig. 3, we present both the experimental and hard sphere structure factors. For manganese, the hard sphere diameter σ_{11} in the alloy is taken to be that of pure manganese σ_1, which has been

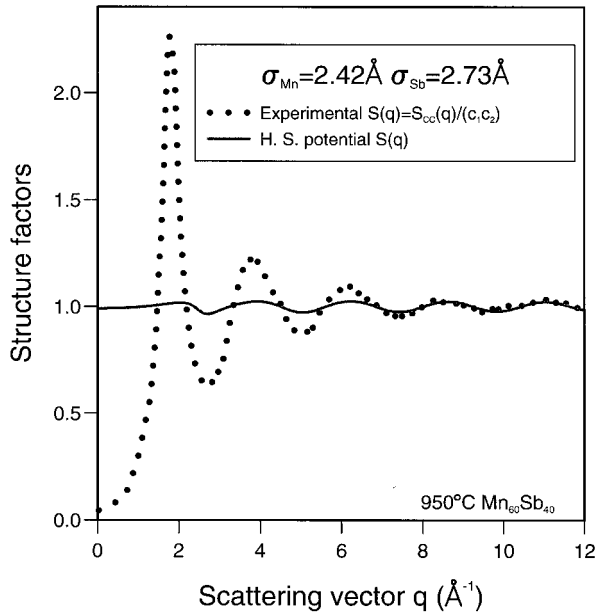

FIGURE 3 Total structure factors obtained from the experiment and from hard spheres for the $Mn_{60}Sb_{40}$ zero alloy at 950°C. The hard sphere diameters are those of the pure metals.

deduced from the packing fraction and from the experimental density of pure manganese. The packing fraction is given by Waseda [21] as a function of temperature: $\eta_i = A_i \exp(-B_i T)$ (the parametes A_i and B_i have been tabulated in table 3-1 of Waseda's book [21]). The density is compiled by Crawley [22] as a function of temperature under the form: $d_i = a_i - b_i(T - T_{Mi})$, T_{Mi} is the melting temperature of the ith pure metal. For antimony, the hard sphere diameter σ_{22} has been determined on our (unpublished) pure metal structure factor measurements of antimony at 950°C [23]. Its temperature behaviour is deduced from the Waseda formula. The value of the hard sphere diameters of pure manganese and antimony are respectively: $\sigma_{Mn} = 2.419$ Å, $\sigma_{Sb} = 2.728$ Å at 950°C and $\sigma_{Mn} = 2.470$ Å, $\sigma_{Sb} = 2.766$ Å at 800°C.

The hard sphere total structure factor is quasi-flat (Fig. 3). The small remaining oscillations come from the difference between the hard sphere diameters of antimony and manganese. The important experimental peak at 1.775 $Å^{-1}$ indicates a very strong chemical interaction traducing heterocoordination. No peaks are observed at 2.175 and 2.800 $Å^{-1}$ where are located the pure manganese and antimony main peaks. This is in contradiction with most of the total structure factors, which are obtained for alloys (where nevertheless in general both metals present a positive neutron diffusion length). We have represented on Fig. 4 the Fourier transform (Eq. (7)) $g_{11}(r) + g_{22}(r) - 2g_{12}(r)$, which traduces either the homocoordination or the heterocoordination. With hard spheres, we obtain above the first hard sphere diameter $\sigma_{Mn} = 2.42$ Å (Fig. 4) a positive peak. Near the half distance (2.58 Å) between the hard sphere diameters σ_{Mn} and σ_{Sb}, the $2g_{12}(r)$ term gives a predominant negative peak. Then above 2.86 Å the curve is quasi-flat. It is clear that the hard sphere model with the hard sphere diameters of pure metals cannot represent the experimental structure factor and pair correlation function.

4.1.1.2 The Hard Sphere Diameters Vary with Concentration To interpret our experimental structure factor, it is necessary to improve the interatomic potentials. In the framework of the hard sphere model, it is possible to consider that the hard sphere diameters are composition dependent. Physically this can be explained by a charge transfer

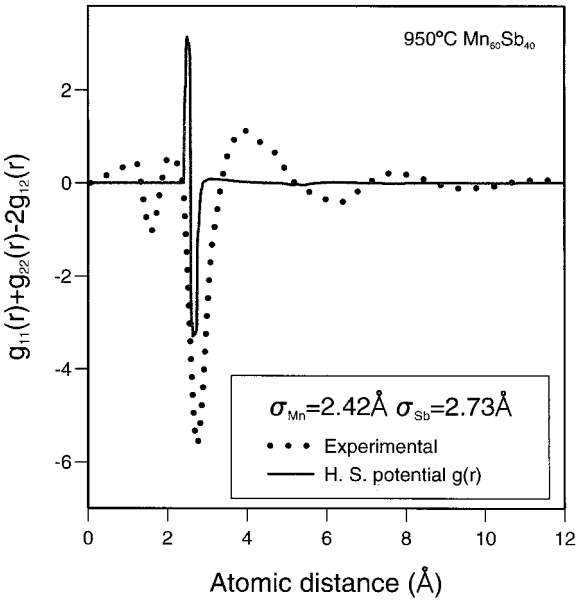

FIGURE 4 Function $g_{11}(r)+g_{22}(r)-2g_{12}(r)$ obtained from the experiment and from hard sphere potentials calculated for the $Mn_{60}Sb_{40}$ zero alloy at 950°C (corresponds to the Fig. 3 structure factors).

from manganese to antimony. The zero alloy is particularly interesting. Indeed Eq. (4) reduces to $g_{tot}(r)-1=c_1c_2(g_{11}(r)+g_{22}(r)-2g_{12}(r))=g_{cc}(r)/(c_1c_2)$ which is the difference between homo and heterocoordination. The effect of a modification of the interatomic potential (of the hard sphere diameter presently) is easily seen on the total structure factor (Fig. 5) and can be interpreted on the $(g_{11}(r)+g_{22}(r)-2g_{12}(r))$ curve, (Fig. 6). With normal alloys each effect is hidden in the total $g_{tot}(r)$ which is weighted by the concentrations and the neutron scattering lengths. With the zero alloy, we immediately see on the $g(r)-1$ curve, the effect of moving the hard sphere diameter or changing the height of the Silbert–Young square well. So we can adjust the parameters of the potential on this curve and see immediately the effects, what cannot be done with non-zero alloys.

The best fit on *simultaneously* the structure factor (Fig. 5) and the pair correlation function (Fig. 6) is obtained with a manganese hard sphere diameter in the alloy ($\sigma_{11}=\sigma_{Mn}$) of 1.85 Å and an antimony

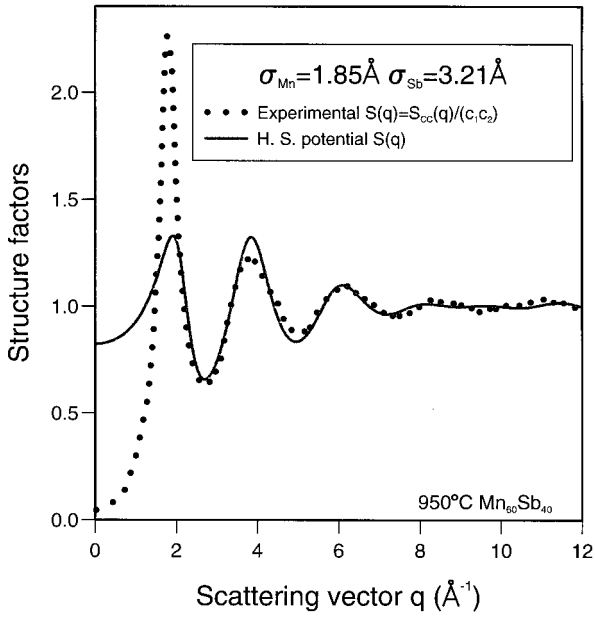

FIGURE 5 Total structure factors obtained from the experiment and from hard sphere potentials calculated with composition dependant hard sphere diameters for the $Mn_{60}Sb_{40}$ zero alloy at 950°C.

diameter ($\sigma_{22} = \sigma_{Sb}$) of 3.21 Å. We choose σ_{11} in order to obtain that the increase of the calculated $g_{11}(r) + g_{22}(r) - 2g_{12}(r)$ function at r equal to 1.85 Å corresponds to the experimental increase. We choose a value of the parameter σ_{12} so that the sharp decrease of the function $g_{11}(r) + g_{22}(r) - 2g_{12}(r)$ occurs at the same r-value than the experimental function. The value of the antimony hard sphere diameter in the alloy σ_{22} is connected to σ_{11} and σ_{12} by the Lorentz-Berthelot rule: $2 \cdot \sigma_{12} = \sigma_{11} + \sigma_{22}$. These changes represent respectively a variation of 24% for the manganese hard sphere diameter in the alloy compared to the pure metal and of 18% for the antimony one. These variations seem very important if one considers that the difference of electronegativity between manganese and antimony is only equal to 0.4 (1.5 for Mn and 1.9 for Sb). Following the Sergent–Welch table of periodic properties of the elements, the ionic character of this alloy is only of 4% with this difference of electronegativities. On Fig. 5, we observe that the agreement between the experimental and calculated structure factors

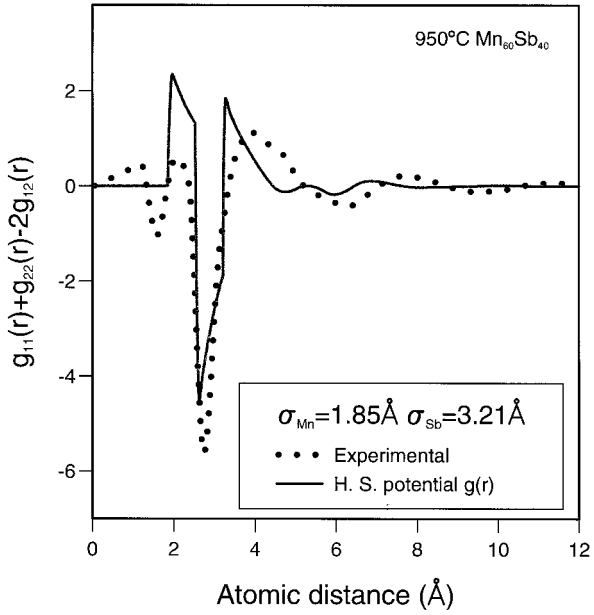

FIGURE 6 Function $g_{11}(r)+g_{22}(r)-2g_{12}(r)$ obtained from the experiment and from hard sphere potentials calculated with composition dependant hard sphere diameters for the $Mn_{60}Sb_{40}$ zero alloy at 950°C (corresponds to the Fig. 5 structure factors).

is bad between 0 and 6 $Å^{-1}$. The low angle limit of the structure factor is very different from the experimental one. The agreement is only acceptable on the second and third peak. Above we observe a shift between the experimental and calculated extremes. On Fig. 6, we compared the experimental and calculated $g_{11}(r)+g_{22}(r)-2g_{12}(r)$ functions. The agreement concerning the position of the sharp rises is good but the calculation fails to realise the fit on the height of the different peaks. We conclude that a hard sphere structure factor alone cannot represent the experiment even if we take into account a drastic modification of the hard sphere diameters with concentration. So it is necessary to refine the model.

4.1.2 Experiment and Shouldered Models

We now come back to the possible shapes of the ab initio interatomic potentials (Figs. 1 and 2). We can observe three regions: a sharp

repulsive potential for small values of r, an intermediate region, which can be either attractive or repulsive, where we find the first nearest neighbours, finally a decreasing oscillatory tail. Three degrees of approximation have been used in order to represent as well as possible the different shapes of the effective potential. In the first one, the repulsive potential is described by the "hard sphere potential". In the second one, the intermediate region can be characterised by the Silbert–Young correction. In our third calculation, we proposed to add a second contribution of the opposite sign as has been represented on Figs. 1 and 2. In this third model, we kept the hard sphere diameters constant in the alloy ($\sigma_{ii} = \sigma_i$; $\sigma_{jj} = \sigma_j$).

4.1.2.1 Silbert–Young Potential with Concentration Dependent Hard Sphere Diameters for Alloys In order to realise a better agreement of $S(q)$ and $g(r)$ with experiment, we use Silbert–Young potentials. The parameters $A_{\mathrm{Mn–Mn}}$, $A_{\mathrm{Mn–Sb}}$ and $A_{\mathrm{Sb–Sb}}$ of the three effective Silbert–Young potentials are determined in order to represent the same drastic change as observed on the experimental $g_{11}(r) + g_{22}(r) - 2g_{12}(r)$ curve. The parameter $\varepsilon_{\mathrm{Mn–Mn}}$ has been determined in order to adjust $g_{11}(r) + g_{22}(r) - 2g_{12}(r)$ between 1.85 and 2.53 Å where the other partial pair correlation functions do not contribute. Then we adjust simultaneously, $\varepsilon_{\mathrm{Mn–Sb}}$ and $\varepsilon_{\mathrm{Sb–Sb}}$ on the maximum of the experimental structure factor (Fig. 7) and on the minimum of the pair correlation function $g_{11}(r) + g_{22}(r) - 2g_{12}(r)$ (Fig. 8). The best values that we obtained at 950°C are:

$$\begin{array}{lll} \sigma_{\mathrm{Mn-Mn}} = 1.85\,\text{Å} & \sigma_{\mathrm{Sb-Sb}} = 3.21\,\text{Å} & \sigma_{\mathrm{Mn-Sb}} = (\sigma_{\mathrm{Mn-Mn}} + \sigma_{\mathrm{Sb-Sb}})/2 = 2.53\,\text{Å} \\ \varepsilon_{\mathrm{Mn-Mn}}/k_{\mathrm{B}}T = 1.70 & \varepsilon_{\mathrm{Sb-Sb}}/k_{\mathrm{B}}T = -0.20 & \varepsilon_{\mathrm{Mn-Sb}}/k_{\mathrm{B}}T = -0.49 \\ A_{\mathrm{Mn-Mn}} = 1.40 & A_{\mathrm{Sb-Sb}} = 1.51 & A_{\mathrm{Mn-Sb}} = 1.28 \end{array} \tag{19}$$

We remark that the parameter ε_{11} is positive (repulsion between manganese atoms) and that both ε_{12} and ε_{22} are negative. The value of the experimental low angle limit $S(0)$ is nearly five times smaller than the calculated one. The agreement is fairly well realised both in

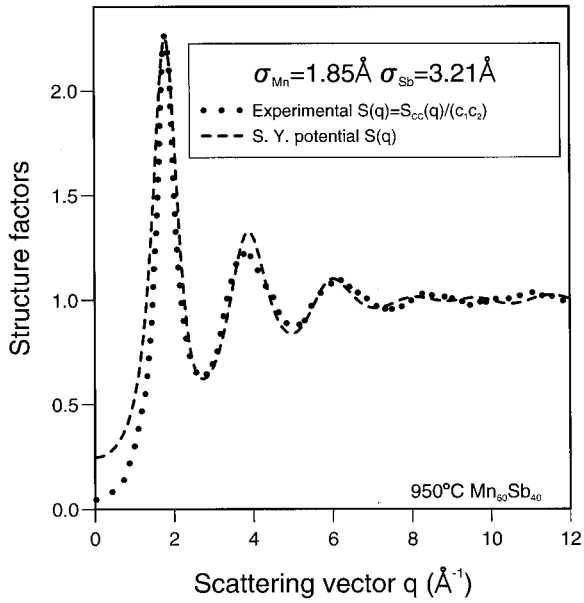

FIGURE 7 Total structure factors obtained from the experiment and from the Silbert–Young potentials with a variation of the hard sphere diameters for the $Mn_{60}Sb_{40}$ zero alloy at 950°C.

the real space and in the reciprocal space. On Fig. 9, we present the corresponding Faber–Ziman partial structure factors. We observe that the important repulsive parameter of the Mn–Mn effective potential leads to a split of the first main peak of $a_{11}(q)$. The attractive parameter Sb–Sb and Mn–Sb enhances the first peak to a value of 2.9 for Sb–Sb (compared to 2.1 with hard spheres) and 2.0 for Mn–Sb (compared to 1.6 for hard sphere). We also observe a deep dip in the $a_{12}(q)$ partial structure factor at 1.8 Å^{-1}. The main peak of $S(q)$ comes essentially from the addition of the $a_{22}(q)$ main peak (maximum at 2.1 Å^{-1}) and from the negative $a_{12}(q)$ prepeak at 1.8 Å^{-1} resulting from the attraction between the two different species. The resulting total structure factor has a main peak at 1.8 Å^{-1}. We present on Fig. 10 the partial pair correlation function (with an expanded scale) and their contribution to $g_{11}(r)+g_{22}(r)-2g_{12}(r)$. The total function obtained is near the experimental one (Fig. 8) except for the sharp rise at the hard sphere diameters which has to be softened. If one admits that there is a charge transfer,

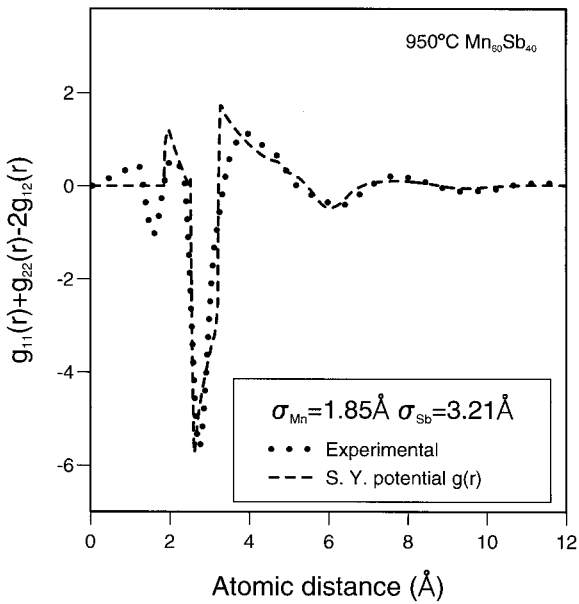

FIGURE 8 Function $g_{11}(r)+g_{22}(r)-2g_{12}(r)$ obtained from the experiment and from Silbert–Young potentials calculated with a variation of the hard sphere diameters for the $Mn_{60}Sb_{40}$ zero alloy at 950°C (corresponds to the Fig. 7 structure factors).

it seems physically logical that the potential between identical atoms (with the same electric charges) presents a repulsive contribution and that it is attractive between unlike atoms. So it seems strange that this fit leads to an attraction between antimony atoms. We can also observe on Fig. 7 that the calculated structure factor is out of phase with the experimental one at high q values. This means that the hard sphere diameters are not adequately chosen. The variations of the hard sphere diameters seem us too important if one considers the small electronegativity difference. For all these reasons this model which gives however an overall agreement, in the intermediate q range, seems not to be adequate.

4.1.2.2 Double Step Potential with Concentration Independent Hard Sphere Diameters Here we propose a model of potential (double step potential) in order to take better into account the real shape of the

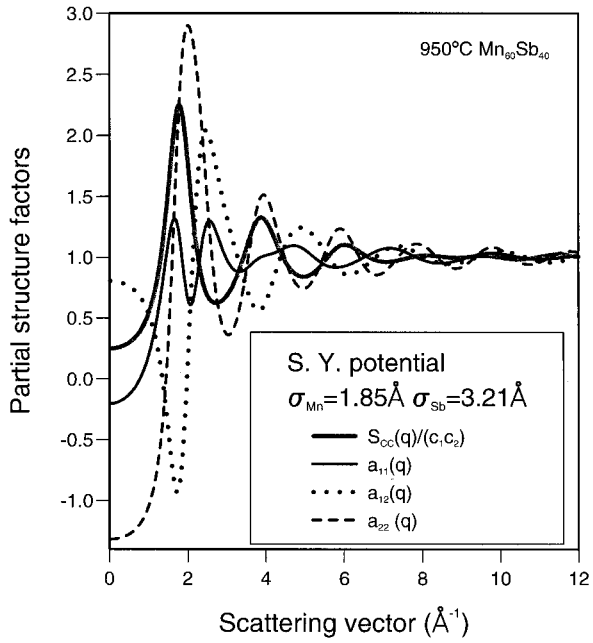

FIGURE 9 Faber–Ziman partial structure factors $a_{ij}(q)$ and Bhatia–Thornton partial structure factor $S_{CC}(q)$ obtained from a Silbert–Young step potentials with a variation of the hard sphere diameters for the $Mn_{60}Sb_{40}$ zero alloy at 950°C (corresponds to the Fig. 7 total structure factors).

potential. From a physical point of view, we consider here that the charge transfer is negligible and thus that the hard sphere diameters in the alloy do not vary with concentration. This assumption was supported by the fact that for large q ($q > 7\,\text{Å}^{-1}$) the hard sphere structure factor represents well the experimental one (Fig. 3). The problem is now to choose the parameters of the double step potentials $\varepsilon_{\text{Mn–Mn}}$, $A_{\text{Mn–Mn}}$, $\varepsilon'_{\text{Mn–Mn}}$, $A'_{\text{Mn–Mn}}$, $\varepsilon_{\text{Sb–Sb}}$, $A_{\text{Sb–Sb}}$, $\varepsilon'_{\text{Sb–Sb}}$, $A'_{\text{Sb–Sb}}$, $\varepsilon_{\text{Mn–Sb}}$, $A_{\text{Mn–Sb}}$, $\varepsilon'_{\text{Mn–Sb}}$ and $A'_{\text{Mn–Sb}}$. We can be helped by the ordering potential concept as has been discussed by Bhatia and Thornton [4]. The ordering effective potential is characterised by the difference $v_{11} + v_{22} - 2v_{12}$. It is clear that we can obtain the same total structure factor and total pair correlation function with different partial potentials v_{ij}, which give the same ordering effective potential. But some potential may be unphysical. For example, we have obtained very good results on the total structure factor and the total pair correlation

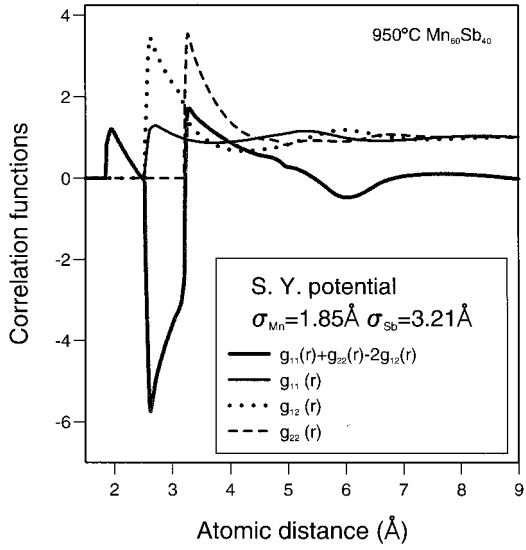

FIGURE 10 Partial pair correlation functions obtained from Silbert–Young potentials with a variation of the hard sphere diameters for the $Mn_{60}Sb_{40}$ zero alloy at 950°C (corresponds to the Fig. 8 total pair correlation functions).

function by considering that the ordering potential which corresponds to the measured $S_{CC}(q)$ and $g_{CC}(r)$, is only concentrated in a v_{12} contribution and that v_{11} and v_{22} are hard sphere potentials. But the partial structure factors are unphysical. For these reasons we split the ordering potential half on a repulsive v_{11} and v_{22} effective potentials, half on an attractive v_{12} potential. In order to reduce the number of independent parameters to four, and to two hard spheres diameters which are the same that for the pure metals, we introduced the following relations and the parameters values at 950°C:

$$\begin{aligned}
\sigma_{\mathrm{Mn-Mn}} &= \sigma_{\mathrm{Mn}} = 2.42\,\text{Å} \\
\sigma_{\mathrm{Sb-Sb}} &= \sigma_{\mathrm{Sb}} = 2.73\,\text{Å} \quad (\sigma_{\mathrm{Mn-Sb}} = (\sigma_{\mathrm{Mn-Mn}} + \sigma_{\mathrm{Sb-Sb}})/2 = 2.58\,\text{Å}) \\
\varepsilon_{\mathrm{Mn-Mn}}/k_{\mathrm{B}}T &= \varepsilon_{\mathrm{Sb-Sb}}/k_{\mathrm{B}}T = -\varepsilon_{\mathrm{Mn-Sb}}/k_{\mathrm{B}}T = 1.12 \\
A_{\mathrm{Mn-Mn}} &= A_{\mathrm{Sb-Sb}} = A_{\mathrm{Mn-Sb}} = 1.20 \\
\varepsilon'_{\mathrm{Mn-Mn}}/k_{\mathrm{B}}T &= \varepsilon'_{\mathrm{Sb-Sb}}/k_{\mathrm{B}}T = -\varepsilon'_{\mathrm{Mn-Sb}}/k_{\mathrm{B}}T = -0.20 \\
A'_{\mathrm{Mn-Mn}} &= A'_{\mathrm{Sb-Sb}} = A'_{\mathrm{Mn-Sb}} = 1.80
\end{aligned} \tag{20}$$

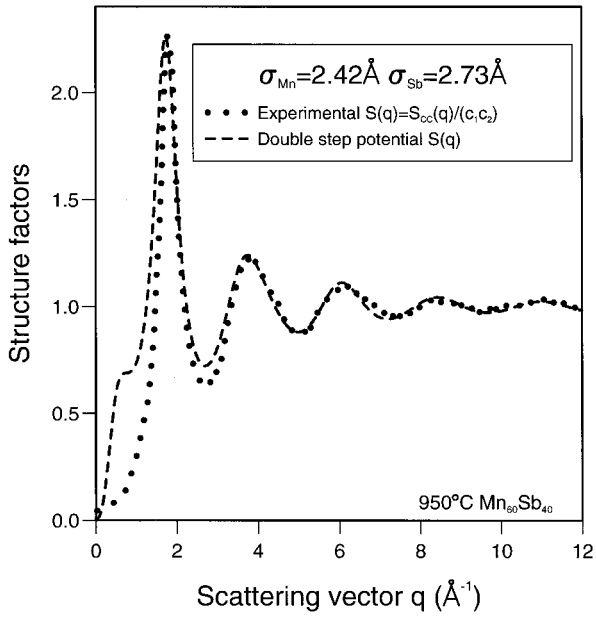

FIGURE 11 Total structure factors obtained from the experiment and from our double step potentials for the $Mn_{60}Sb_{40}$ zero alloys at 950°C.

The total structure factor is represented in Fig. 11 while the total pair correlation function is plotted in Fig. 12. The main peak of the structure factor as well as the oscillations at high q are very well represented by this model with these parameters. The small angle limit is nearly the same than the experimental one. The only difference occurs near $0.8\,\text{Å}^{-1}$ where our model presents a hump. The $g(r)$ curves are also very similar and fit better the experimental curve than all previous models. An important difference with the precedent model can be noticed on Fig. 12 around 2 Å where in this case the positive value of the experimental $g(r)$ is not considered as having a physical meaning but being an artefact of the Fourier transform of the experimental structure factor.

We have plotted in Fig. 13 the Faber–Ziman double step potential partial structure factors together with the total one. We observe the traditional main peaks, which have vanished in $S(q) = S_{CC}(q)/(c_1c_2)$. Theirs values are lower than 2.5 and are physically acceptable. Due to the negative diffusion length of manganese, the partial structure

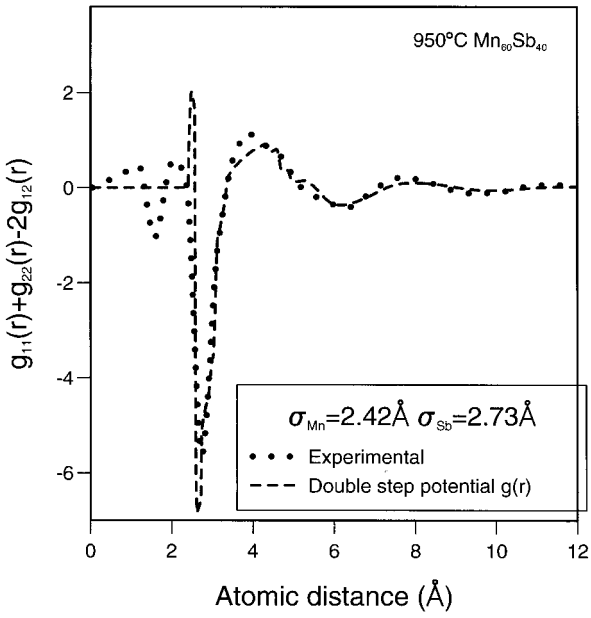

FIGURE 12 Function $g_{11}(r)+g_{22}(r)-2g_{12}(r)$ obtained from the experiment and from our double step potentials for the $Mn_{60}Sb_{40}$ zero alloys at 950°C (corresponds to the Fig. 11 structure factors).

factor main peaks are cancelled by the linear combination of partial structure factors and the prepeak is magnified. The remaining oscillations at high q value come from incomplete cancellation due to the slightly different position of the peaks related to the different hard sphere diameters. Sometimes one can observe some prepeaks on the total structure factors as for example for Ni–Al or Ni–Al–Si [14] where we have even used the Silbert–Young potential to explain qualitatively the prepeak. This is clearly observed on Fig. 13, where we reproduce fairly well the main peak (which is in fact a magnified prepeak).

Nevertheless we have a small shoulder on the left side of our calculated prepeak. This shoulder comes from the second step of our effective potentials. In the Fourier transform, it is clear that further steps of the potential bring contributions which neutralise this hump.

In Fig. 12, we see that our model represents pretty well the first minimum in the $g_{11}(r)+g_{22}(r)-2g_{12}(r)$ function, the maximum after is less

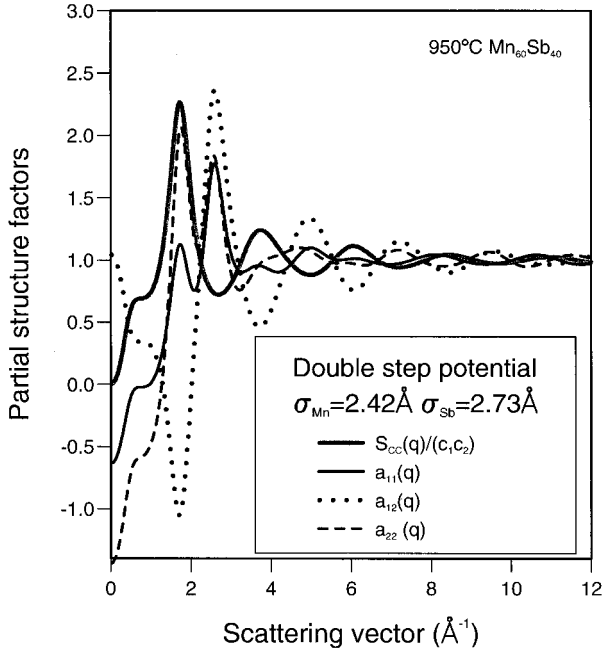

FIGURE 13 Faber–Ziman partial structure factors $a_{ij}(q)$ and Bhatia–Thornton partial structure factor $S_{CC}(q)$ obtained from our double step potentials for the $Mn_{60}Sb_{40}$ zero alloy at 950°C (the hard sphere diameters are those of the pure metals).

accurately described but very much better than with hard spheres and with earlier models. The experimental $g_{11}(r)+g_{22}(r)-2g_{12}(r)$ (Fig. 12) is negative in the range 2.42–3.24 Å and shows clearly the heterocoordination. The calculated curve obtained by the double step potential presents two peaks, one positive the second negative. The first one is located between σ_{Mn} and σ_{Mn-Sb}; the second one between σ_{Mn-Sb} and σ_{Sb}. The calculated minimum value (-6.85) of the function $g_{11}(r)+g_{22}(r)-2g_{12}(r)$ is 1.22 below the experimental one (-5.63). These differences are due to the hardness of the hard sphere potential. We can emphasise that they will vanish with smoother real effective potentials. We have presented on Fig. 14 the different partial pair correction functions where we show clearly the different contributions and the effects of the partial correlation functions $g_{ij}(r)$ in the quantity $g_{11}(r)+g_{22}(r)-2g_{12}(r)$. It can be seen that the $g_{12}(r)$ function weighted by a factor -2 is responsible of the deep minimum in the total function

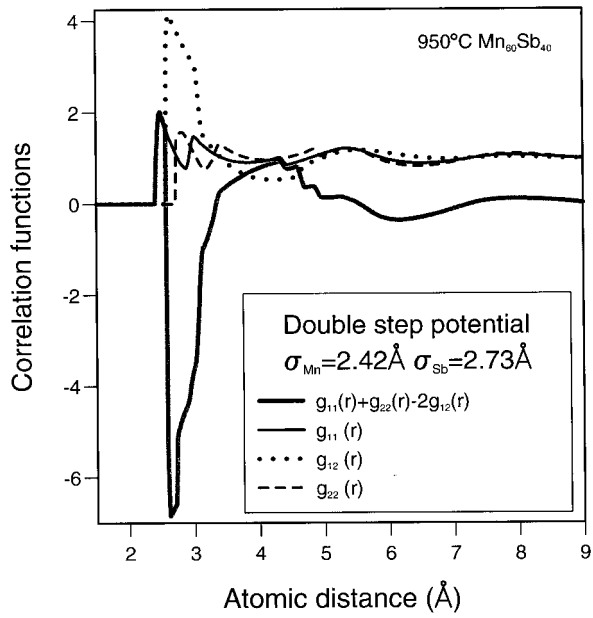

FIGURE 14 Partial pair correlation functions obtained from our double step potentials for the $Mn_{60}Sb_{40}$ zero alloy at 950°C (corresponds to the Fig. 12 pair correlation functions).

between 2.42 and 3.24 Å. This explains clearly the heterocoordination of this alloy, which is due simultaneously to an attractive potential between unlike atoms and a repulsive potential between identical atoms. Of course, the remaining differences between the experimental value and our calculated curve can perhaps even be improved. For this, it is necessary to take into account a softer potential near the hard sphere diameters and further oscillations of the interatomic potentials. We believe however that the most important physical contributions are included in the present calculation.

4.1.3 Discussion

With a zero alloy, the situation is different from classical alloys because the main peaks are neutralised and that other parts of the structure factor are magnified. If we return to the characteristic shapes of the ab initio interatomic potentials that have been given in

Figs. 1 and 2, we observe that at large distances, the interatomic potentials oscillate with decreasing amplitude. At small distance we have a very important repulsive potential (hard sphere potential). At intermediate distances we observe either an attractive potential (like for Al–Al) or a repulsive one (like for Ge–Ge). The parameters have been adjusted in order to obtain simultaneously a good total structure factor (like in Fig. 11) and a good Fourier transform (like in Fig. 12). The effects of the different contributions of the potentials are more visible on Fig. 12 because we work in the same r space than the potential. It is clear on Fig. 13 that the main peak of the experimental structure factor comes from a combination of prepeaks of the Mn–Mn and Sb–Sb partial structure factors and from a minimum of Mn–Sb partial structure factor. All these peaks (positive or negative) are at the same q value ($\cong 1.8\mathring{A}^{-1}$). The potentials of the Figs. 1 and 2 have been obtained for normal metals. But the pseudopotentials are inadequate to describe transition metal alloys and cannot be used for the Mn–Sb alloy. Hafner *et al.* [12] obtained realistic total structure factors with a mean Yukawa potential for the liquid alloy (using the ordering potential concept). This shows that one can obtain a good total structure factor if the difference between identical *ii* or *jj* interactions and unlike *ij* interaction is correct. We have obtained a very good total structure factor (results not presented here) with a very simpler assumption i.e., by taking hard spheres for *ii* or *jj* interactions and a square well attractive potential only for the *ij* interatomic potential. This needs only four independent parameters (σ_1, σ_2, A_{12} and ε_{12}). In that case the partial structure factors are not realistic because the depth of the attractive well potential is too important. The partial structure factors which have a height of their main peak of about 5 are not physically acceptable. This kind of discussion can only be held if the partial structure factors are plotted! In the present work, we prefer replace the important attractive potential *ij* by a less attractive *ij* interaction and repulsive *ii* and *jj* contributions which seems us more physical. More accurate fits can only be obtained if one has more experimental information (for example if one has experimental partial structure factors).

We have seen that two very different models can explain nearly as well the intermediate range of the experimental structure factor. The low and high q limits are better reproduced with constant hard

sphere diameters. The hump in the 0.5–0.8 Å^{-1} range obtained with the double step potential is not observed experimentally. A careful analysis shows that this hump comes from the second square well contribution, which may be corrected by higher oscillations of the potential.

The problem is to examine what is the more realistic situation and to appeal to other physical properties than structural ones. In the charge transfer situation, a good result is obtained with a very important change of the hard sphere diameters (except for low and high q values where the calculated structure factors are out of phase). The difference in the electronegativity (0.4) is small and it seems us improbable that we have an ionic situation in the alloy. The experimental resistivity (250 $\mu\Omega$ cm) is not characteristic of an ionic conductivity. We do not believe to an important charge transfer for the manganese antimony alloy.

4.2 Structure Factor of $Mn_{40}Sb_{60}$

We measured also the structure factor of $Mn_{40}Sb_{60}$ at 800°C (Fig. 15) which is no more a zero alloy. We have observed an increasing of the midheight width of the structure factor main peak (midheight width 0.54 Å^{-1} for $Mn_{40}Sb_{60}$ and 0.33 Å^{-1} for $Mn_{60}Sb_{40}$ at 950°C). We have calculated the total structure factor with all models described before. Figure 15 shows the hard sphere and the double step potential structure factors with concentration independent hard sphere diameters. The hard sphere diameters have been changed in order to take into account their temperature dependence ($\sigma_{Mn} = 2.47$ and $\sigma_{Sb} = 2.77$ Å). The hard sphere potential main peak appears at 2.35 Å^{-1} for the hard sphere potential while for the experiment it is observed at 1.9 Å^{-1}. The double step potential represents well the oscillatory behaviour of the structure factor and gives the good main peak width but overestimate a little its values.

The calculation with concentration dependent hard sphere diameters is presented on Fig. 16. We only change the hard sphere diameters by fitting on the experimental $S(q)$. We obtain with less accuracy the value $\sigma_{Mn} = 2.0$ and $\sigma_{Sb} = 3.0$ Å. With these values we represented well the oscillatory behaviour of the structure factor. They correspond respectively to variations equal to 19 and 10% of the

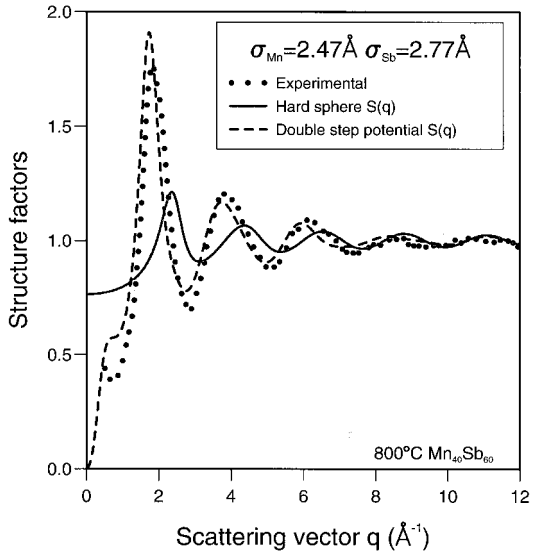

FIGURE 15 Experimental, hard sphere and double step total structure factors for the $Mn_{40}Sb_{60}$ at 800°C with pure metal hard sphere diameters.

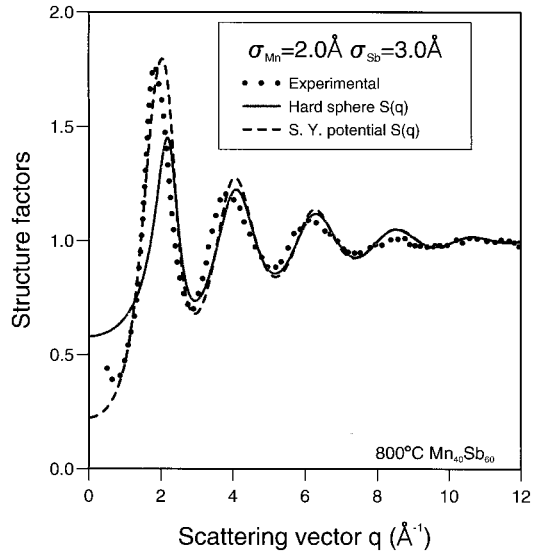

FIGURE 16 Experimental, hard sphere and Silbert–Young total structure factors for the $Mn_{60}Sb_{40}$ at 800°C with variation of the hard sphere diameters.

hard sphere diameters. These variations are less important than those of $Mn_{60}Sb_{40}$ alloy. In this model, the "chemical effect" is less pronounced for this concentration in spite of a lower temperature. The other parameters are the same than those used for $Mn_{40}Sb_{60}$. There is a pretty good agreement between the experiment and the structure factor calculated from the Silbert–Young potential with a diameter change. However, the same physical arguments than for the $Mn_{60}Sb_{40}$ zero alloy can be used (electronic transport properties and repulsive antimony–antimony repulsive potential) to prefer the double step potential with constant hard sphere diameters.

5 CONCLUSION

In this paper, we have presented experimental results of neutrons scattering on molten manganese–antimony alloys. The null matrix method allowed us to observe directly a strong chemical order. We have discussed different models to interpret the experimental structure factor. It is clear that the hard sphere potential cannot explain the structure even with concentration dependent hard sphere diameters. The intermediate q range can be explained nearly as well either by a "Silbert–Young" potential (first model with a change in hard sphere diameters on alloying) or by an attractive potential between unlike ions described by our "double step" potential with concentration independent hard sphere diameters. The nature of the alloy is very different in the two cases. In the first model, it is not reasonable to accept physically the attraction of the antimony–antimony effective potential and the high q oscillations are not reproduced. The ionic character, corresponding to a charge transfer model, is not described in the electronic transport properties. Finally, we have concluded that the variation of the hard sphere diameters must be very small and that it exist an attraction between unlike atoms and repulsion between identical atoms (heterocoordination). This explains well the experimental results and corresponds also to a better understanding of the physics of such alloys. Good results are also obtained for $Mn_{40}Sb_{60}$ and show the coherence of this interpretation.

We hope than further theoretical work in this field with effective potentials obtained from transition metal pseudopotentials will be

able to describe our experimental structure factor with an ab initio formalism.

Acknowledgements

We would like to thank CNI/MAT and particularly M. Dubuit, B. Menette and H. Rouxel for computation help, J.C. Humbert for technical assistance in making the experimental cells used in this work, J.P. Ambroise for this technical help during the neutron experiment.

References

[1] J.G. Gasser and R. Kleim (1977). *Inst. Phys. Conf. Ser.*, **30**, 352.
[2] N. Benazzi (1998). Thèse de Doctorat d'Etat. Université d'Oujda Morocco.
[3] O. Dreirach, R. Evans, H.-J. Güntherodt and H.-U. Künzi (1972). *J. Phys. F: Met. Phys.*, **2**, 709.
[4] A.B. Bhatia and D.E. Thornton (1970). *Phys. Rev.*, **B2**, 3004.
[5] H. Ruppersberg and H. Reiter (1982). *J. Phys.: Met. Phys.*, **12**, 1311.
[6] N.W. Ashcroft and D.C. Langreth (1967). *Phys. Rev.*, **156**, 500.
[7] T.E. Faber (1972). *An Introduction to the Theory of Liquid Metals*. Cambridge at the University Press.
[8] L.S. Ornstein and F. Zernike (1914). *Proc. Acad. Sci. Amsterdam*, **17**, 793.
[9] J.K. Percus and G.J. Yevick (1958). *Phys. Rev.*, **110**, 1.
[10] M. Silbert and W.H. Young (1976). *Phys. Lett.*, **27**, 469.
[11] R.V. Gopala and B.M. Satpathy (1982). *Phys. Stat. Sol.*, (b) **110**, 273.
[12] J. Hafner, A. Pasturel and P. Hicter (1984). *J. Phys. F: Met. Phys.*, **14**, 2279.
[13] J.L. Lebowitz (1964). *Phys. Rev.*, **133**, A895.
[14] S. Saadeddine, J.F. Wax, B. Grosdidier and J.G. Gasser (1994). *Phys. Chem. Liq.* **28**, 221.
[15] N. Koubaa and J.G. Gasser (1990). *J. Non-Cryst. Solids*, **117**/**118**, 316.
[16] G.B. Bachelet, D.R. Hamann and D. Schlüter (1982). *Phys. Rev.*, **B26**, 4199.
[17] J.P. Ambroise, M.C. Bellissent-Funel and R. Bellissent (1984). *Revue Phys. Appl.*, 731.
[18] M.C. Bellissent-Funel (1977). Thèse de Doctorat d'Etat. Université de Grenoble France.
[19] Ji-Chen Li, N. Cowlam and F. He Fenglai (1988). *Phys. Chem. Liq.*, **18**, 31.
[20] G.E. Bacon (1975). *Neutron Diffraction*. Oxford Claredon.
[21] Y. Waseda (1980). *The Structure of Non-Crystalline Materials*. Mac Graw Hill, New York.
[22] A.F. Crawley (1974). *Int. Met. Rev.*, **19**, 32.
[23] B. Grosdidier. Pure antimony structure factor. *Internal Report*.